Measurement report: Rapid oxidation of phenolic compounds by O₃ and HO•: effects of air-water interface and mineral dust in tropospheric chemical processes

Yanru Huo[a], Mingxue Li[b], Xueyu Wang[c], Jianfei Sun[d], Yuxin Zhou[a],

Yuhui Ma[a], Maoxia He[a],*

[a] Environment Research Institute, Shandong University, Qingdao 266237,

P. R. China

[b] Department of Civil and Environmental Engineering, The Hong Kong

Polytechnic University, Hong Kong SAR, China

[c] College of Geography and Environmental Sciences, Zhejiang Normal

University, Jinhua 321004, China

[d] School of Environmental and Materials Engineering, Yantai University,

Yantai, 264005, PR China

_____

*Corresponding author: Prof. Maoxia He

Tel: 86-532-58631972 (o)

Fax: 86-532-5863 1986

E-mail address: hemaox@sdu.edu.cn

Abstract

Environmental media affect the atmospheric oxidation processes of phenolic compounds (PhCs) released from biomass burning in the troposphere. Phenol (Ph), 4-hydroxybenzaldehyde (4-HBA), and vanillin (VL) are chosen as model compounds to investigate their reaction mechanism and kinetics at the air-water (A-W) interface, on TiO_2 clusters, in the gas phase, and in bulk water using a combination of molecular dynamics simulation and quantum chemical calculations. Of them, Ph was the most reactive one. The occurrence percentages of Ph, 4-HBA, and VL staying at the A-W interface are ~72%, ~68%, and ~73%, respectively. As the size of $(TiO_2)_n$ clusters increases, the adsorption capacity decreases until $n > 4$, and beyond this, the capacity remains stable. A-W interface and TiO_2 clusters facilitate Ph and VL reactions initiated by the O_3 and $HO^\bullet$, respectively. However, oxidation reactions of 4-HBA are little affected by environmental media because of its electron-withdrawing group. The O_3- and $HO\bullet$-initiated reaction rate constant (k) values follow the order of $Ph_{A\text{-}W} > VL_{TiO_2} > VL_{A\text{-}W} > 4\text{-}HBA_{A\text{-}W} > 4\text{-}HBA_{TiO_2} > Ph_{TiO_2}$ and $VL_{TiO_2} > Ph_{A\text{-}W} > VL_{A\text{-}W} > 4\text{-}HBA_{TiO_2} > Ph_{TiO_2} > 4\text{-}HBA_{A\text{-}W}$, respectively. Some byproducts are more harmful than their parent compounds, so should be given special attention. This work provides key evidence for the rapid oxidation observed in the $O_3/HO^\bullet$ + PhCs experiments at the A-W interface. More importantly, differences in oxidation of PhCs by different

45 environmental media due to the impact of substituent groups were also

46 identified.

47 **Keywords:** Air-water interface; Titanium dioxide (TiO$_2$); Phenolic

48 Compounds; Adsorption mechanism; Molecular dynamics (MD).

49 **1. Introduction**

50   Biomass burning, stemming from natural wildfires and human activity,

51 significantly contributes to atmospheric particulate matter (PM). Biomass

52 burning is a primary source of approximately 90% of the global primary

53 organic aerosols (POA) and releases a substantial quantity of organic

54 pollutants (Ito and Penner, 2005; Chen et al., 2017; Chen et al., 2023).

55 Biomass burning is to blame for about 62% of total annual emissions of

56 about 8.0 Tg of black carbon and 93% of total annual emission of about

57 33.9 Tg of organic carbon worldwide (Bond et al., 2004). Emissions from

58 biomass combustion are one of the primary sources of atmospheric and

59 particle pollutants that negatively affect human health, air quality, and

60 climate (Reid et al., 2005; Yao et al., 2016). One of the three main types of

61 biopolymers responsible for the formation of biomass is lignin (Sun et al.,

62 2011), also the polymeric organic molecule most abundant in plants (Lou

63 et al., 2010; Soongprasit et al., 2020). Pyrolysis of lignin releases phenolic

64 compounds (PhCs) into the air, including phenols, phenolic aldehydes, and

65 methoxyphenols. By mass, these PhCs make up between 21% and 45% of

66 the aerosol composition (Hawthorne et al., 1989; Diehl et al., 2013; Liao

67 et al., 2020; Soongprasit et al., 2020). Methoxyphenols are one of the

68 potential tracers that can be found in atmospheric wood smoke pollution,

69 with the emission rate ranging from 900 to 4200 mg kg^{-1} fuel (Hawthorne

70 et al., 1989; Rogge et al., 1998; Simoneit, 2002; Chen et al., 2017).

71 Evidence shows that the oxidation processes of PhCs can result in the

72 formation of secondary organic aerosol (SOA) (Yee et al., 2013; Jiang et

73 al., 2023). Hence, it is imperative to explore the effects of PhCs when

74 exposed to atmospheric oxidants.

75   After being released into the atmosphere, PhCs will be oxidized by

76 ozone (O_3) and hydroxyl radicals (HO$^{\bullet}$). Both are significant contributors

77 to SOA. The homogenous oxidation of PhCs has been the emphasis of

78 previous studies (Henry et al., 2008; Yee et al., 2013; Liu et al., 2019;

79 Arciva et al., 2022). Researchers investigated the kinetics and reaction

80 mechanisms of gas-phase interactions of PhCs with O_3 and HO$^{\bullet}$ in the past

81 decade (Kroflič et al., 2018; Smith et al., 2016; Sun et al., 2021a; Sun et

82 al., 2021b; Liu et al., 2022). Furthermore, they investigated the

83 hydroxylation, ring opening, and oligomerization processes of PhCs in the

84 atmospheric liquid phase, with a focus on the potential environmental

85 toxicity and climatic effects of these events (Liu et al., 2022; Arciva et al.,

86 2022; Carena et al., 2023).

87   However, there is a dearth of specific data as well as explanations of

88 the mechanisms involved in the atmospheric oxidation of PhCs at the air-

89   water (A-W) interface. The atmosphere contains a high concentration of

90   aqueous aerosols and water microdroplets (Zhong et al., 2019). The

91   oxidation of PhCs can rapidly occur at A-W interface. The term "water

92   surface catalysis" denotes the phenomenon where chemical reactions

93   happen at a faster rate at A-W interface compared to the bulk phase (Lee

94   et al., 2015a; Lee et al., 2015b; Yan et al., 2016; Banerjee et al., 2017). In

95   chemical engineering, titanium dioxide (TiO_2) is an essential photoactive

96   component found in atmospheric mineral dust (Sakata et al., 2021; Wang

97   et al., 2023). The interaction between PhCs and TiO_2 is continuous

98   (Grassian, 2009; Rubasinghege et al., 2010; Shang et al., 2021), despite the

99   relatively low prevalence of TiO_2 mineral particles (comprising 0.1% to 10%

100 by mass). Therefore, it is essential to investigate the disparity in the

101 oxidation reaction mechanisms and kinetics of PhCs at A-W interface and

102 mineral dust particles.

103   Phenol (Ph), 4-hydroxybenzaldehyde (4-HBA), and vanillin (VL) are

104 selected as model compounds to present comprehensive mechanistic

105 information at A-W interface, on TiO_2 clusters, in the gas phase, and in

106 bulk water, using a combination of molecular dynamics simulation and

107 quantum chemical calculations. Rate constants were measured throughout

108 a wide temperature range in various EM. Additionally, computational

109 toxicology was employed to evaluate the ecotoxicological impact of PhCs

110 and their transformation products.

2. Methods

2.1 Molecular dynamics simulation

All of the molecular-dynamics simulations were carried out by utilizing the GROMACS 2019 package, which included the AMBER force field. Parametrization of the Ph, 4-HBA, and VL was accomplished by using the GAFF force field in conjunction with RESP charge calculations performed at the M06-2X/6-311++G(3df,2p)//M06-2X/6-31+G(d,p) level. The TIP3P water model was utilized so that individual water molecules may be represented (Jämbeck and Lyubartsev, 2014).

2.1.1 Properties of Ph, 4-HBA, and VL at the A-W interface

Considering the significance of the interfacial behavior of Ph, 4-HBA, and VL at the A-W interface, the properties of these three substances were initially examined by focusing on the A-W interface. **Fig. S1 (a)** depicts a rectangular box that has dimensions of $4 \times 4 \times 9$ nm^3 and has a Z-axis that is perpendicular to the A-W contact. This box was used for all simulations. To begin the process of constructing the initial configurations, a water slab measuring $4 \times 4 \times 4$ nm^3 was positioned at the coordinates (2 nm, 2 nm, 4.5 nm) of the center of mass (COM). Because the rest extension along the Z-axis of the box was sufficiently large (2.5 nm^3), it was possible to steer clear of the intersection of two A-W interface. Prior to the formal simulation, six Ph molecules were randomly placed in a vacuum above the

132 water box for 150 nanoseconds of NVT molecular-dynamics simulations.

133 The results show that there are no significant π-π interactions or formation

134 of hydrogen bonds between the Ph molecules. To simplify the model, this

135 was followed by simulations of individual molecules. Ph, 4-HBA, or VL

136 were each placed in their own compartment at the coordinates (2.0 nm, 2.0

137 nm, 7.75 nm) for each system in order to simulate the behavior of these

138 molecules in the gas-water interface region of nanobubbles. To begin, the

139 three different systems were optimized to use the least amount of energy

140 possible. After that, NVT molecular-dynamics simulations were carried

141 out for a total of 150 nanoseconds.

142 *2.1.2   Umbrella sampling simulations*

143 In **Fig. S1 (b)**, the molecule of Ph, 4-HBA, or VL was placed inside the

144 box (their COM is (2.00 nm, 2.00 nm, 6.00 nm)), which is located directly

145 2.00 nm away from the COM of the water slab. The distance between the

146 COM of Ph, 4-HBA, or VL and that of the water slab was used as the

147 definition for the reaction coordinate. The weighted histogram analysis

148 approach, also known as WHAM, can be used to calculate the free energy

149 profiles of Ph, 4-HBA, or VL when they transition from the gas phase into

150 bulk water (Kumar et al., 1992; Hub et al., 2010). **Text S1** has an

151 explanation of the specifics.

152 *2.1.3   Radial distribution function*

153 Estimating the strength of hydrogen bonds (HB) between specific

154 atoms can be done with the help of a tool known as the radial distribution

155 function (RDF). **Text S2** has an explanation of the specifics.

156 *2.2 DFT calculations*

157   In this work, all calculations pertaining to the electrical structure were

158 accomplished by utilizing the Gaussian16 program (Frisch et al., 2016). By

159 benchmarking   at   the   CCSD(T)/cc-pVDZ,   CBS-QB3,   B3LYP/6-

160 311+G(d,p), MP2/6-311+G(d,p) and M06-2X/6-311+G(d,p) levels, Cao et

161 al. (Cao et al., 2021) found that M06-2X/6-311++G(3df,2p)//M06-2X/6-

162 31+G(d,p) is reliable for PhCs. Therefore, all calculations for gas-phase

163 reactions are performed at this level. **Text S3** contains a description of the

164 additional calculated details. Multiwfn (Lu and Chen, 2012) was used to

165 construct the electron density map. This program integrates Visual

166 Molecular Dynamics (version 1.9.3) (Humphrey et al., 1996) in order to

167 conduct an analysis of the electrostatic potential (ESP) and the average

168 local ionization energy (ALIE).

169 *2.3 IRI analysis*

170   Interaction Region Indicator (IRI) (Lu and Chen, 2021) was used to

171 determine the chemical bonds and weak interactions of Ph/4-HBA/VL

172 adsorbed to TiO_2 clusters (the details are in **Text S4**).

173 *2.4 Kinetic calculations*

174   **Text S5** contains an explanation of the kinetic calculations.

175 **3. Result and discussion**

3.1 Enrichment of Ph, 4-HBA, and VL at the A-W interface

3.1.1 The uptake of gaseous PhCs at the A-W interface

Fig. S1 and **Fig. S2** illustrate the relative distributions of water, O_3, and PhCs molecules (Ph, 4-HBA, and VL) in the A-W interface system along the z-axis. $HO^{•}$ are primarily situated at the A-W interface contact, with the potential to diffuse through the water slab interior (Roeselová et al., 2004). **Fig. 1(a)** displays the variation in water density along the Z-coordinate distance from 0 to 9 nm, categorizing three zones: A-W interface (2.25 to 2.79 nm and 6.21 to 6.75 nm), air (0 to 2.25 nm and 6.75 to 9 nm), and bulk water (2.79 to 6.21 nm). This method accurately determines the interfacial range (Zhang et al., 2019; Shi et al., 2020). According to location definitions, O_3 percentage distribution was as follows: 26% at the A-W interface; 72% in the air; and 2% in pure water (**Fig. 1(b)**). **Fig. 1(c)** depicts MD trajectories of Ph diffusion through the water slab from the air region over a 150 ns period. Ph is distributed in the air (8%) and bulk water (20%), with the majority at the A-W interface (72%) (**Fig. 1 (d)**). The majority of 4-HBA and VL molecules are located at the A-W interface, constituting 68% and 73% of the total locations as presented in **Fig. S2**.

In **Fig. 2(a)**, we observe the three key processes involving PhCs (Ph, 4-HBA, or VL) diffusing into the water slab from the air region. (I) The mutual attraction of gaseous Ph, 4-HBA, or VL and nanoparticles; (II) The uptake of PhCs (Ph, 4-HBA, or VL) at the air-nanoparticle interface; (III)

198   The hydration reaction of PhCs (Ph, 4-HBA, or VL) in the bulk water. **Fig.**

199   **2(b)** displays the free energy profile of the trajectories as Ph/4-HBA/VL

200   transitions from the air into the bulk water (see **Text 6** for calculations

201   details). The $\Delta G_{gas \rightarrow interface}$ values are -0.22 kcal mol $^{-1}$ for the Ph-A-W

202   (Phenol-Air-Water) system, -0.45 kcal mol $^{-1}$ for the 4-HBA-A-W (4-

203   hydroxybenzaldehyde-Air-Water) system, and -0.20 mol $^{-1}$ for the VL-A-

204   W (Vanillin-Air-Water) system. These values suggest that it is

205   thermodynamically favorable for PhCs to approach the interfacial water

206   molecules. **Fig. S3** illustrates typical snapshots from the trajectories of

207   PhCs (Ph, 4-HBA, or VL). Initially, one molecule of Ph, 4-HBA, or VL

208   was placed in the center of the water box, with an equivalent COM distance

209   of 2 nm between the PhCs and the air phase. Subsequently, the PhCs moved

210   closer to the interface, leading to adsorption at the A-W interface. During

211   the adsorption process, the H atom of phenolic hydroxyl group served as

212   an electron donor, binding to the oxygen atom on the surface and

213   preventing its return to the bulk water. Concurrently, hydrogen bonds were

214   formed. This property allowed the phenolic hydroxyl groups on PhCs can

215   effectively adhere to the A-W interface, consistent with the experimental

216   observations using steady-state interfacial vibrational spectra (Kusaka et

217   al., 2021). Based on these findings, the location where air and water meet

218   exhibits an increased concentration of PhCs.

219   *3.1.2   Interface properties of PhCs*

220   The research focused on understanding the behavior of PhCs at A-W

221   interface. The distribution probability of angle (α, β, γ) for Ph/4-HBA/VL

222   in relation to the A-W interface is shown in **Fig. 3(a)–(d)**. The Z-axis is

223   defined as the axis perpendicular to the interface. The angles are formed

224   between the Z-axis and the benzene ring plane, the phenolic hydroxyl

225   group, and the O–αC bound of Ph, 4-HBA, and VL, respectively, denoted

226   as α, β, and γ. In the Ph-A-W, 4-HBA-A-W, and VL-A-W systems, a broad

227   distribution range is observed, suggesting that PhCs are rather randomly

228   distributed across the interface. However, statistically, the highest

229   distribution range for α and β falls within 15°–25° (or 145°–165°) and

230   75°–95°, respectively. This applies to both α and β. In the VL-A-W system,

231   the highest distribution range for α is around 93°. In general, introducing

232   more hydrophilic functional groups increases the characteristic angle α and

233   β of PhCs at the interface, allowing for more secure adsorption at the water-

234   air interface.

235   To set up the interface reaction environment for further quantum

236   chemical calculations, the radial distribution function (g(r)) of Ph, 4-HBA,

237   and VL at interfaces was computed and is show in **Fig. 3 (e)–(g)**. These

238   figures also display the radial distribution function (RDF) and the

239   coordination number N of H_{Ph-OH}–O_{H_2O}, $H_{4-HBA-OH}$–O_{H_2O}, and H_{VL-OH}–O_{H_2O}

240   at the A-Winterface. Peak intensities are observed in the range of 0.25–0.3

241   Å for H_{Ph-OH}–O_{H_2O}, $H_{4-HBA-OH}$–O_{H_2O}, and H_{VL-OH}–O_{H_2O}, as shown in **Fig.**

242 **3(e)–(g)**, respectively. The interaction between H_{PhCs} and O_{H_2O} is the

243 primary factor influencing the stability of PhCs at the interface. The N

244 values of $H_{Ph\text{-}OH}$–O_{H_2O}, $H_{4\text{-}HBA\text{-}OH}$–$O_{H_2O}$, and $H_{VL\text{-}OH}$–O_{H_2O} are 2.68, 2.51,

245 and 2.09 respectively. The number of functional groups attached to the

246 benzene ring affects the N value; more functional groups lead to a lower N

247 value. When a molecule has more functional groups, it occupied more

248 space and exerts a stronger repulsive force on the nearby water molecules

249 compared to those with fewer functional groups.

3.2 Adsorption of Ph, 4-HBA, and VL by TiO₂ Clusters

250

251 The investigation into the structural stability of TiO_2 clusters (Zhai and

252 Wang, 2007; Syzgantseva et al., 2011; Arab et al., 2016) has revealed six

253 distinct types of $((TiO_2)_n$ (n = 1–6)) clusters as depicted in **Fig. S4**. The

254 structural parameter values computed for TiO_2 clusters using the M06–

255 2X/6-31+G(d,p)/LANL2DZ level align with reported experimental values

256 (Calatayud et al., 2008; Bai et al., 2020). **Fig. 4, S5, and S6** provide

257 additional insights into the adsorption of PhCs on $(TiO_2)_n$ (n = 1–6) clusters.

258 The placement of PhCs on TiO_2 clusters significantly impacts adsorption

259 energies (Bai et al., 2020). The adsorption capacity of pollutants on cluster

260 surfaces is a key factor influencing degradation efficiency (Qu and Kroes,

261 2006). The primary mechanism of phosphorus atoms adsorption to $(TiO_2)_n$

262 (n = 1–4) clusters occurs at a range of 2.57 to 2.61 Å and involves

263 interaction between the $H_{\text{-}OH}$ atom and the O_{TiO_2} atom, as seen in **Fig. 4(a)**.

264 Hydrogen bonds can be formed between the H_{-OH} atom and the O_{TiO_2} atom

265 (1.80–2.61 Å), improving the adsorption capacity. In contrast, Ph

266 adsorption to $(TiO_2)_n$ (n = 5–6) clusters, ranging from 2.08 to 2.09 Å, is

267 primarily due to interaction between Ti atom and O_{-OH} atom. In **Fig. S5**,

268 the primary interaction for 4-HBA and VL occurs between the Ti atom and

269 the O_{-CHO} atom, with distances ranging from 1.93 and 2.07 Å. TiO_2 clusters

270 have a greater potential to interact with the oxygen atom of the aldehyde

271 group than with the oxygen atom of the phenolic hydroxyl group. **Fig. S7**

272 presents the ALIE surface values for the three PhCs considered. Lower

273 ALIE values indicate weaker binding of electrons, with darker blue regions

274 signifying the lowest local minimum ALIE levels. ALIE values, in the

275 range of 11.42–11.97 eV, for O_{-CHO} atom are lower than those for O_{-OH} atom

276 (12.49−15.46 eV) or O_{-OCH_3} atom (14.96 eV) due to the electron-accepting

277 nature of the aldehyde group. Therefore, the interaction between the

278 titanium atom and O_{-CHO} atom is stronger than with the O_{-OH} or O_{-OCH_3}

279 atoms.

280 Adsorption energy a metric of adsorption capacity, is illustrated in **Fig.**

281 **4(b)–(d)** for phosphorus, 4-hydroxybenzoic acid, and vinylidene

282 dichloride on $(TiO_2)_n$ (n = 1–6). TiO_2 exhibits the highest adsorption

283 capacity for PhCs. ($\Delta G_{ad} = -72.35$ kcal mol^{-1}) (**Fig. 4(b)**). The adsorption

284 energy difference values of TiO_2 and $(TiO_2)_3$ for 4-HBA and VL are −45.32

285 (**Fig. 4(c)**) and −102.46 kcal mol^{-1} (**Fig. 4(d)**), respectively. The energy of

286   physorption range from −1.20 to 9.56 kcal mol $^{-1}$ illustrates the

287   spontaneous chemical adsorption (Nollet et al., 2003). However, the

288   capacity of TiO_2 to adsorb VL is significantly higher than that to adsorb Ph

289   and 4-HBA. **Fig. 4(b)−(d)** show that the adsorption capacity falls as the

290   size of TiO_2 clusters increases when n ≤ 4. In contrast, the adsorption

291   capacity remains constant when n > 4. IRI measurements of Ph on the

292    $(TiO_2)_n$ surface (**Fig. 4(e)**) reveal Ph-TiO_2 hydrogen bonds (H_{Ph}−O_{TiO_2}

293   bonds bonds) and their electrostatic and dispersion effects. Benzene C atom

294   exhibits sp^2 hybridization, meaning it forms one σ-bond and one π-bond.

295   The sp^2 hybridization of benzene explains its limited interaction with TiO_2

296   clusters and accounts for the substantial adsorption energy. Similar

297   interactions occur with 4-HBA and VL (**Fig. S6**). Hydrogen bonds form

298   between the H_{-CHO} atom of 4-HBA or VL and the O_{TiO_2} atom, despite the

299   presence of the H_{Ph} atom.

3.3 Continuous oxidation mechanisms

3.3.1 O_3- and HO•-initiated reactions

302   PhCs, once released into the atmosphere, undergo several processes,

303   including adsorption on mineral aerosol surfaces, accumulation at the A-W

304   interface, dispersion in bulk water within liquid droplets, and oxidation

305   reactions initiated by atmospheric oxidants. This section delves into the

306   detailed mechanisms and characteristics of these reactions. At the M06-

307   2X/6-311++G(3df,2p)//M06-2X/6-31+G(d,p) level, the structures with the

308 minimum free energy for the Ph/4-HBA/VL has been determined (**Fig. S9**).

309 In the case of VL, a significant reduction in molecular energy is observed

310 due to the formation of a powerful intramolecular hydrogen bond with a

311 length of 2.09 Å between the H and O atoms near the methyl group.

312 Moreover, the lone pair electrons of oxygen atoms can form additionally

313 p-π conjugations with the π electrons of the phenyl ring, further reducing

314 the overall energy of VL. The statistical charts of calculated $\Delta_r G$ and $\Delta G^{\ddagger}$

315 values for O_3- and $HO^{\bullet}$-initiated reactions are displayed in **Fig. 5** and **S8**

316 and detailed data are available in **Tables 1–4**.

317   O_3 is a major oxidant in the atmosphere, with high concentrations in

318 the troposphere ranging between 7×10^{11} molecules cm $^{-3}$ (Platt et al., 1984;

319 Prinn et al., 1995b). Investigating the fate of PhCs in the presence of O_3 is

320 essential. The ozonolysis of PhCs involves the synthesis of primary

321 ozonide, the formation of active Criegee intermediate (CI), and the

322 disintegration of CI. The O_3-initiated reactions of Ph/4-HBA/VL involve

323 radical adduct formation (RAF) channels on the benzene ring ($R_{O_3\text{-RAF}}1-$

324 6), highlighted in red in **Fig. S9**. **Fig. 5(a)–(d)** depict that the ozonolysis

325 pathways $R_{O_3\text{-RAF}}$ are exergonic, indicating their spontaneity. The average

326 $\Delta G^{\ddagger}$ values for the ozonolysis of Ph/4-HBA/VL are ranked as Ph > VL >

327 4-HBA. The following is a list of the average values for the ozonolysis of

328 Ph/4-HBA/VL, as illustrated in **Fig. 5(e)**–**5(h)**, Ph is superior to VL and 4-

329 HBA, with the exception on TiO_2 clusters. **Fig. 5(e)** illustrates that the

330   average value of $\Delta G^{\ddagger}$ for O_3 + Ph reactions at the A-W interface is 15.38

331   kcal mol^{-1}, the lowest value out of the three PhCs. The average $\Delta G^{\ddagger}$ values

332   for the ozonolysis of Ph/4-HBA/VL are as follows: VL (13.95 kcal mol^{-1})

333   < Ph (24.70 kcal mol^{-1}) < 4-HBA (25.16 kcal mol^{-1}) on TiO_2 clusters (**Fig.**

334   **5(f)**). The average $\Delta G^{\ddagger}$ values for O_3 + VL reactions in gas phase are the

335   highest among the four different EM (23.28 kcal mol^{-1}) shown in **Fig.**

336   **5(g)**). Comparing the phenolic oxidation in each of these four EM (bulk

337   water, interface, TiO_2 clusters, and gas phase) reveals that A-W interface

338   are more conducive to the ozonolysis of Ph, whereas TiO_2 clusters are more

339   conducive to the ozonolysis of VL. The effect of solvation on $\Delta G^{\ddagger}$ is

340   predominantly caused by the hydration of the phenolic OH group, as this

341   is the part of the molecule being dissolved. However, the presence of water

342   molecules in the region around the phenyl group has been shown to have a

343   considerable influence on the $\Delta G^{\ddagger}$ values.

344   HO$^{\bullet}$, known as "atmospheric detergents", is another significant

345   atmospheric oxidant (Atkinson, 1986; Zhang et al., 2020). According to

346   research by Prinn (Prinn et al., 1995a), the worldwide average

347   concentration of HO$^{\bullet}$ during 12 hours per day is roughly 1.6×10^6

348   molecules cm^{-3}. For this reason, elucidating the reaction mechanism

349   underlying O_3 + PhCs reactions in the troposphere is of the utmost

350   importance. HO$^{\bullet}$-initiated reaction pathways of Ph/4-HBA/VL include

351   RAF, hydrogen atom abstraction (HAA) channels from the benzene ring

352 (R_{HAA}ben1–6) and the substituent group (R_{HAA}sub7–9). Previous research

353 (Gao et al., 2019) has shown that the process of single electron transfer

354 (SET) does not significantly contribute to the $HO^{\bullet}$-initiated reactions

355 examined. Once the hydroxyl adducts or H_2O are formed, significant heats

356 (4.21–30.28 kcal mol $^{-1}$) are released (**Fig. 5(i)–(l), S8 (a)–(d) and (i)–(l);**

357 the detail data in **Table S3**), indicating high thermodynamic feasibility. The

358 average $\Delta G^{\ddagger}$ values for $HO^{\bullet}$-initiated reactions (**Fig. 5(m)–(p), S8 (e)−(h)**

359 and **(m)–(p))** are lower than those for O_3-initiated reactions. Routs

360 R_{HAA}ben make a minimal contribution to $HO^{\bullet}$-initiated reactions. At the A-

361 W interface, VL (3.52 kcal mol $^{-1}$) < Ph (4.52 kcal mol $^{-1}$) < 4-HBA (9.50

362 kcal mol $^{-1}$), and the $\Delta G^{\ddagger}$ value of Ph is the lowest (-0.97 kcal mol $^{-1}$), the

363 case for pathways R_{RAF-HO}• (**Fig.5(m)**). Among the three aromatic

364 compounds, the R_{RAF-HO}• routes of VL on TiO_2 clusters are the most

365 favorable (**Fig. 5(n)**). When compared to $HO^{\bullet}$-initiated reactions of

366 aromatic compounds in the gas phase (**Fig. S8(e)**) or bulk water (**Fig. S8(f)**),

367 the process of Ph + $HO^{\bullet}$ reactions at the A-W interface is accelerated,

368 whereas the process of VL + $HO^{\bullet}$ reactions is accelerated by TiO_2 clusters.

369 These findings are in agreement with the ozonolysis findings. The same

370 guidelines can be used to routes R_{HAA}sub (**Fig. 5(o), (p), S8 (g) and (h)**)

371 and R_{HAA}ben (**Fig. S(m)−(p)**). The following is a ranking of the average

372 $\Delta G^{\ddagger}$ values for routes R_{RAF-HO}• in the gas phase or bulk water: Ph < 4-HBA

373 < VL. As a result of having the lowest $\Delta G^{\ddagger}$ values among all $HO^{\bullet}$-initiated

374 reaction mechanisms, routes R_{RAF} are the most advantageous of all the

375 possible reaction mechanisms. In light of this, each and every route R_{RAF-}

376 $_{HO}\bullet$ and R_{HAA}sub will be dissected in detail.

377 **Fig. 6** shows the $\Delta_r G$ and $\Delta G^{\ddagger}$ values of O_3- and $HO^{\bullet}$-initiated reactions

378 at various reaction locations. These reactions are almost entirely

379 exothermic, with a close correlation between $\Delta_r G$ values and $\Delta G^{\ddagger}$ values.

380 The $\Delta G^{\ddagger}$ values for the Phe $+ O_3$ reactions shown in **Fig. 6(a)** are the lowest

381 among the three compounds, ranging from -0.97 to 7.86 kcal mol $^{-1}$.

382 Exergonic and spontaneous addition reactions took place at the C1$-$C2 and

383 C3$-$C4 locations of Ph and VL, respectively. Because of their low $\Delta G^{\ddagger}$

384 values, the C1$-$C2 and C2$-$C3 sites of O_3-initiated reactions for 4-HBA are

385 advantageous. Their values are 21.76 and 22.03 kcal mol $^{-1}$, respectively.

386 The C1$-$C2 location of 4-HBA is activated to a greater extent at the A-W

387 interface in comparison to the gas phase and bulk water. However, the $\Delta G^{\ddagger}$

388 values of $O_3 +$ Ph reactions on TiO_2 clusters are significantly greater than

389 those of the A-W interface ($12.86-18.10$ kcal mol $^{-1}$) than $24.30-25.34$

390 kcal mol $^{-1}$. The VL $+ O_3$ reactions on TiO_2 clusters are favorable at the

391 C2$-$C3 and C4$-$C5 locations (the $\Delta G^{\ddagger}$ values are 11.42 and 11.14 kcal mol

392 $^{-1}$, respectively, **Fig. 6(b)**). This can be explained by the fact that the

393 electron cloud has a greater propensity to congregate in the places C2$-$C3

394 and C4$-$C5, respectively. In addition, the p orbitals of the methoxy and

395 hydroxy groups are conjugated to the benzene ring, which offers a

396   powerful electron-donating conjugation effect (Aracri et al., 2013).

397   Because of this, the oxidation of aromatic molecules is thermodynamically

398   more favorable than the oxidation of the aldehyde group. Clearly, the $\Delta G^{\ddagger}$

399   values of HO$^{\bullet}$-initiated reactions (-0.97–13.46 kcal mol^{-1}) in **Fig. 6(c)–(f)**

400   are lower than those of O_3-initiated processes (11.14–27.83 kcal mol^{-1}) at

401   different points in A-W interface and TiO_2 clusters. This can be seen by

402   comparing the values to each other. At the A-W interface, the most

403   advantageous position for the phenol hydroxyl group to be in for Ph/4-

404   HBA/VL + HO$^{\bullet}$ reactions are the ortho position (**Fig. 6(c)**). OESI-MS,

405   which stands for online electrospray ionization mass spectrometry, was

406   also able to identify the hydroxylation product known as 3,4-

407   dihydroxybenzaldehyde (Rana and Guzman, 2020). In **Fig. 6(d)**, the ortho-

408   and meta-sites of phenol hydroxyl are, respectively, the most favorable

409   positions for Ph/4-HBA + HO$^{\bullet}$ reactions on the TiO_2 clusters. On the other

410   hand, all of the VL sites on the TiO_2 clusters are advantageous. At the A-W

411   interface and on the TiO_2 clusters, the abstraction of hydrogen atoms

412   follows the order of H_{CHO} atom > H_{OCH_3} atom > H_{OH} atom in **Fig. 6(e)**

413   **and (f)**. This can also be explained by the ALIE values of these atoms listed

414   in the same order of H_{CHO} atom (11.67–11.74 eV) > H_{OCH_3} atom (14.06

415   eV) > H_{OH} atom (15.46 eV), as shown in **Fig. S7**.

416   ***3.3.2 Generation and degradation of key products***

417   For the purpose of this discussion, the primary atmospheric destiny of

418   the selected aromatic compounds was taken into consideration to be their

419   bimolecular reactions with O_2/O_3. **Fig. 7** and **S10** illustrate the subsequent

420   reaction mechanisms of IMs, respectively. IM_{1-2} was produced using the

421   pathway that offered the best conditions for the HO$^{•}$-initiated reaction of

422   Ph. As can be seen in **Fig. 7(a)**, the addition of O_2 to the C3 sites of the

423   C_6H_5O radicals results in the formation of C_6H_5O-OO with no barriers in

424   either the gas phase or the bulk water. This is a desirable outcome. For the

425   transformation of the $C_6H_5O_2$-OO radicals that were created, the ring

426   closure reaction to form $C_6H_5O_2$-OO-d is the most attractive option.

427   However, it must overcome an energy barrier of 18.83 kcal mol $^{-1}$ in the

428   gas phase or 13.67 kcal mol $^{-1}$ in bulk water. The $C_6H_5O_2$-OO-d_1 radical,

429   which was produced by the $C_6H_5O_2$-OO-d reaction, interacts once more

430   with O_2. Malealdehyde (P1) is what should mostly result from the reaction

431   of the $C_6H_5O_2$-OO-d_1 radical with NO. However, during this process, it still

432   needs to overcome an energy barrier of 49.5 (in the gas phase) or 50.83

433   kcal mol $^{-1}$ (in the bulk water) to generate $C_6H_5O_2$-OO-d_3 radical; as a

434   result, the further transformation of the formed $C_6H_5O_2$-OO-d_2 should

435   continue very slowly. Pyrocatechol (P2) is the primary product generated

436   in the gas phase and bulk water when the H atom of the $C_6H_5O_2$-OO radical

437   is displaced. At the A-W interface, a sequence of hydroxylation products,

438   including pyrocatechol (P2), benzene-1,2,3-triol (P3), and benzene-

439   1,2,3,4,5,6-hexaol (P4), are generated through hydroxylation processes

440   rather than by a single SET ($\Delta G^{\ddagger}$ = 111.79 kcal mol $^{-1}$). OESI-MS was also

441   able to identify these hydroxylation products (Rana and Guzman, 2020). In

442   order to gain a more comprehensive understanding of the reaction

443   mechanism at the A-W interface, the major product (the $C_7H_5O_2$ radical)

444   for pathways R_{HAA} of 4-HBA was also taken into consideration. According

445   to **Fig. S10(a)**, the addition of HO$^{\bullet}$ to the C7 sites of the $C_7H_5O_2$ radical

446   can occur without any obstructions. The overpowering of the 18 kcal mol

447    $^{-1}$ barrier resulted in the formation of the hydroxylation products (4-

448   hydroxybenzoic acid (P5), 3,4-dihydroxybenzoic acid (P6), 2,3,4-

449   trihydroxybenzoic acid (P7), and 2,3,4,5,6-pentahydroxybenzoic acid

450   (P8)). There was found to be one transition route for the continued

451   ozonolysis of the hydroxylation products that were produced in P6. The

452   C2–C3 site of P6 to create P6-5O_3 ($\Delta G^{\ddagger}$ = 16.59 kcal mol $^{-1}$) has the lowest

453   activation energy of all the available paths for the relevant reactions (**Fig.**

454   **S10(b)**). This corresponds to a value of 16.59 kcal mol $^{-1}$. When the $\Delta G^{\ddagger}$

455   values of the breakage of five-membered rings created by ozonolysis

456   pathways are compared, one can get the conclusion that the formation of

457   IM_{P6}-5O_3-a is the most favored pathway. All of the hydrogen abstraction

458   processes involving H_2O and IM_{P6}-5O_3-a have rather high energy barriers

459   (32.93 kcal mol $^{-1}$). On the other hand, the very low $\Delta G^{\ddagger}$ values of the -

460   NO-O abstraction make it a desirable choice. Following a chain of

461 ozonolysis reactions, the following products were obtained: ((2E,4Z)-2-

462 formyl-4,5-dihydroxy-6-oxohexa-2,4-dienoic   acid   (P9);   2,3-

463 dihydroxymalealdehyde (P10); and 2,3-dioxpropanoic acid (P11).

464 Therefore, the product that was created, P10, may also be the product that

465 was discovered through experimentation (mass to charge ratios (m/z) = 115)

466 (Rana and Guzman, 2020).

467 *3.4 Comparison with available experimental results*

468   The rate constants (k) of the overall reaction under the temperature

469 range of 278–318 K were computed based on acquired potential energy

470 surfaces for the O$_3$-initiated and HO$^{\bullet}$-initiated reactions of selected

471 compounds. The results of these calculations are listed in **Table S5 and S6**,

472 respectively. The temperature dependences of the various k values for Ph,

473 4-HBA, and VL at the A-W interface and in bulk water are depicted in **Fig.**

474 **8**. At low values of k, there is a positive dependence on temperature. When

475 the k values are raised to a certain degree, the temperature dependency

476 seems to lose any significance it may have had before. The following is an

477 order of the k values for O$_3$-initiated reactions: Ph$_{A-W}$ > VL$_{TiO_2}$ > VL$_{A-W}$ >

478 4-HBA$_{A-W}$ > 4-HBA$_{TiO_2}$ > Ph$_{TiO_2}$ (**Fig. 8(a)**). According to **Fig. 8(b)**, the k

479 values of HO$^{\bullet}$-initiated reactions go as follows: VL$_{TiO_2}$ > Ph$_{A-W}$ > VL$_{A-W}$ >

480 4-HBA$_{TiO_2}$ > Ph$_{TiO_2}$ > 4-HBA$_{A-W}$. If we look at **Fig. 8(a)** and **Fig. 8(b)**, we

481 can see that the k values of HO$^{\bullet}$-initiated reactions are one hundred times

482 greater than those of O$_3$-initiated reactions. **Table 1** is a listing of the

483   experimental and estimated k values that are available for O_3-initiated and

484    $HO^{\bullet}$-initiated reactions at 298 K. According to the findings, the ozonolysis

485   of Ph was promoted by the water-gas interface as well as by TiO_2 clusters,

486   and the $HO^{\bullet}$ initiated reactions of VL were promoted by TiO_2 clusters.

487   However, the O_3/$HO^{\bullet}$ + 4-HBA reactions have the lowest k values among

488   the three molecules when tested in a variety of environmental

489   environments. The estimated k_{O_3+Ph} values at the A-W interface are 11

490   orders of magnitude greater than those of catechol under dry conditions in

491   gas phase (Zein et al., 2015), when compared with the experimental data.

492   Because it has a higher k_{O_3} value, catechol, which is one of the main

493   products of Ph's oxidation in the atmosphere, has a higher degree of

494   reactivity than its parent compound (**Table 1**). The estimated value of VL

495   is lower than the experimentally determined value of k_{O_3} for guaiacol under

496   dry conditions, which is $(0.40 \pm 0.31) \times 10^{-18}$ cm^3 molecule^{-1} s^{-1} in the

497   gas phase (Zein et al., 2015). The difference between the predicted value

498   of $k_{HO^{\bullet}+VL}$ is 1.14×10^{-10} cm^3 molecule^{-1} s^{-1} and the average experimental

499   value of $k_{HO}\bullet$ for methoxyphenols is just an order of magnitude. As a

500   consequence, the findings of our calculations are reliable.

501   *3.5 Ecotoxicity assessment*

502   We made predictions about the ecotoxicity of Ph, 4-HBA, and VL to

503   three different trophic levels of aquatic creatures (fish, daphnia, and green

504   algae) in order to better understand how the atmospheric oxidation process

505 affects aquatic organisms, specifically fish, daphnia, and green algae. The

506 acute toxicity of Ph, 4-HBA, and VL to aquatic organisms follows the order

507 indicated in **Fig. S11(a)**, which is "green algae > daphnid > fish."

508 According to the criteria in **Table S7**, the acute toxicity of Ph, 4-HBA, and

509 VL is either "very toxic" or "toxic" for three aquatic organisms at

510 concentrations ranging from 2.40–27.70 mg L $^{-1}$. The transformation

511 products have a greater average acute toxicity dosage to three aquatic

512 creatures than their parent chemicals did (0.79–1.33 mg L $^{-1}$), as shown by

513 the fact that the transformation products have a value of 1.40–2.82 mg L $^{-1}$.

514 On the other hand, the acute toxicity of some products, such as P1 (0.26–

515 1.00 mg L $^{-1}$) and P10 (0.54 mg L $^{-1}$ to "green algae"), is higher than that

516 of their parent chemicals. On the other hand, **Fig. S11(b)** demonstrates that

517 the sequence of "green algae > fish > daphnid" is the one that has the

518 highest average chronic toxicity. In addition, the longterm toxicity of

519 transformation products is often detrimental, but it is lower than that of the

520 parent chemicals. On the other hand, the chronic toxicity of P1, P2, P3, and

521 P11 is still "toxic/very toxic" to green algae, fish, and daphnid.

522 Consequently, there remains a concern regarding the potential hazards

523 associated with certain transformation products.

524 **4. Conclusions**

525 Combining molecular dynamic simulations (with the AMBER force

526 field) and quantum chemical calculations (at the M06–2X/6–

311++G(3df,2p)//M06–2X/6-31+G(d,p) level) methods has provided

comprehensive insights into the surface properties of Ph, 4-HBA, and VL,

as well as their reactions induced by O_3 and $HO^{\bullet}$, both in homogeneous and

heterogeneous environments. Here are some key findings from this

research:

(1) Free energy well of Ph, 4-HBA, and VL favor the A-W interface as

their preferred location, with the occurrence percentages of approximately

~72%, ~68%, and ~73% respectively. Ph and 4-HBA show a preference for

the A-W interface over the air, with energy difference of around 0.22 and

0.45 kcal mol $^{-1}$. The VL adsorbed on the TiO_2 clusters has a higher

likelihood of remaining compared to VL adsorbed at the A-W interface. (2)

The adsorption capacity of TiO_2 clusters decreases with increasing cluster

size until n > 4. After that point, the adsorption capacity remains constant.

Strong electrostatic attractive interactions and attractive dispersion effects

occur between the benzene of the Ph and Ti atoms. Hydrogen bonds form

between the atom of O_{TiO_2} and the H_{-CHO} group of 4-HBA or VL. (3) The

O_3- and $HO^{\bullet}$-initiated reactions for Ph and VL are facilitated by the A-W

interface and TiO_2 clusters, respectively, For O_3-initiated reactions at the

A-W interface, the C1–C2 position on the benzene ring is most favorable.

In both the A-W interface and on TiO_2 clusters, the total branching ratio for

routes R_{RAF} and R_{HAA}sub is 72.68% ~ 100%. For route R_{HAA}sub, the order

is H_{-CHO} atom > H_{-OCH_3} atom > H_{-OH} atom. (4) The k values (in

549 molecules·cm^{-3} s^{-1}, at 298K and 1 atm) of O$_3$-initiated reactions follow

550 the order of Ph$_{A-W}$ (5.98×10^{-7}) > VL$_{TiO_2}$ (3.30×10^{-15}) > VL$_{A-W}$ (1.27×10

551 $^{-17}$) > 4-HBA$_{A-W}$ (6.79×10^{-23}) > 4-HBA$_{TiO_2}$ (5.32×10^{-24}) > Ph$_{TiO_2}$ (1.84

552 $\times 10^{-24}$). The k values of HO$^•$-initiated reactions follow the order of VL$_{TiO_2}$

553 (6.70×10^{-6}) > Ph$_{A-W}$ (2.69×10^{-6}) > VL$_{A-W}$ (1.73×10^{-7}) > 4-HBA$_{TiO_2}$

554 (3.16×10^{-9}) > Ph$_{TiO_2}$ (3.17×10^{-10}) > 4-HBA$_{A-W}$ (9.49×10^{-11}). (5) Toxicity

555 risk assessment on aquatic species reveal that most of the reaction products

556 are significantly less harmful than the parent compounds. However,

557 products P1, P2, P3, P10, and P11 are more hazardous, and further

558 investigation of their atmospheric fate is recommended.

559   Ph undergoes transformation to malealdehyde and catechol when

560 exposed to O$_3$ or HO$^•$ in the troposphere. When Ph/VL is at the droplet

561 aerosol interface, rapid oxidation to polyhydroxylated compounds occurs.

562 VL eventually creates tiny molecule aldehydes and acids. This oxidation

563 process is accelerated when VL is encased in a mineral aerosol represented

564 by TiO$_2$ clusters. It is recommended that enterprises producing lignin, such

565 as those in the pulp and paper industry, or factories that employ lignin in

566 the manufacturing of adhesives, rust inhibitors, color dispersants, diluents,

567 or other similar products, be constructed in regions with low relative

568 humidity. It is recommended that treatment facilities that collect lignin

569 pyrolysis products and recycle the byproducts be located in the surrounding

570 area.

Data availability

Data related to this article are available online at https://doi.org/10.5281/zenodo.10614650.

Author contributions

Yanru Huo contributed to the manuscript conceptualization, methodology, software, formal analysis, investigation, and writing of the original manuscript. Mingxue Li provided insight into the writing ideas throughout the article. Xueyu Wang offered some guidance on the method section of the manuscript. Jianfei Sun, Yuxin Zhou, and Ma Yuhui reviewed the original manuscript. Maoxia He: Conceptualization, Resources, Writing – review & editing, Supervision, Funding acquisition.

Competing interests

The contact author has declared that none of the authors has any competing interests.

Acknowledgements

Reference

Arab, A., Ziari, F., and Fazli, M.: Electronic structure and reactivity of $(TiO_2)_n$ (n=1–10) nano-clusters: Global and local hardness based DFT study, Comp Mater, 117, 90-97, https://doi.org/10.1016/j.commatsci.2016.01.031, 2016.

593   Aracri, E., Tzanov, T., and Vidal, T.: Use of Cyclic Voltammetry as an

594   Effective Tool for Selecting Efficient Enhancers for Oxidative

595   Bioprocesses: Importance of pH, Ind Eng Chem Res, 52, 1455-1463,

596   https://doi.org/10.1021/ie3027586, 2013.

597   Arciva, S., Niedek, C., Mavis, C., Yoon, M., Sanchez, M. E., Zhang, Q., and

598   Anastasio, C.: Aqueous ·OH Oxidation of Highly Substituted Phenols as

599   a Source of Secondary Organic Aerosol, Environ. Sci. Technol., 56,

600   9959-9967, https://doi.org/10.1021/acs.est.2c02225, 2022.

601   Atkinson, R.: Kinetics and mechanisms of the gas-phase reactions of the

602   hydroxyl radical with organic compounds under atmospheric conditions,

603   Chem. Rev, 86, 69-201, https://doi.org/10.1021/cr00071a004, 1986.

604   Bai, F.-Y., Ni, S., Ren, Y., Tang, Y.-Z., Zhao, Z., and Pan, X.-M.: DFT

605   analysis on the removal of dimethylbenzoquinones in atmosphere and

606   water environments: ·OH-initiated oxidation and captured by $(TiO_2)_n$

607   clusters (n = 1–6), J Haz Mat, 386, 121636,

608   https://doi.org/10.1016/j.jhazmat.2019.121636, 2020.

609   Banerjee, S., Gnanamani, E., Yan, X., and Zare, R. N.: Can all bulk-phase

610   reactions be accelerated in microdroplets?, Analyst, 142, 1399-1402,

611   https://doi.org/10.1039/C6AN02225A, 2017.

612   Bond, T. C., Streets, D. G., Yarber, K. F., Nelson, S. M., Woo, J.-H., and

613   Klimont, Z.: A technology-based global inventory of black and organic

614   carbon emissions from combustion, J Geophys Res-Atoms, 109,

615   https://doi.org/10.1029/2003JD003697, 2004.

616   Calatayud, M., Maldonado, L., and Minot, C.: Reactivity of $(TiO_2)_n$ Clusters

617   (n = 1−10): Probing Gas-Phase Acidity and Basicity Properties, J Phys

618   Chem C, 112, 16087-16095, https://doi.org/10.1021/jp802851q, 2008.

619   Cao, H., Wang, K., Yang, Z., Wu, S., and Han, D.: Quantum chemical study

620   on the ozonolysis mechanism of guaiacol and the structure-reactivity

621   relationship of phenols with hydroxyl, methoxy, and methyl substituents,

622   Chem. Eng.J., 420, 127629, https://doi.org/10.1016/j.cej.2020.127629,

623   2021.

624   Carena, L., Zoppi, B., Sordello, F., Fabbri, D., Minella, M., and Minero, C.:

625   Phototransformation of Vanillin in Artificial Snow by Direct Photolysis

626   and   Mediated   by   Nitrite,   Environ.   Sci.   Technol.,

627   https://doi.org/10.1021/acs.est.3c01931, 2023.

628   Chen, J., Li, C., Ristovski, Z., Milic, A., Gu, Y., Islam, M. S., Wang, S., Hao,

629   J., Zhang, H., and He, C.: A review of biomass burning: Emissions and

630   impacts on air quality, health and climate in China, Sci Total Environ,

631   https://doi.org/10.1016/j.scitotenv.2016.11.025, 2017.

632   Chen, P., Li, Y., Zhang, Y., Xue, C., Hopke, P. K., and Li, X.: Dynamic

633   Changes of Composition of Particulate Matter Emissions during

634   Residential Biomass Combustion, Environ. Sci. Technol., 57, 15193-

635   15202, https://doi.org/10.1021/acs.est.3c05412, 2023.

636   Diehl, B. G., Brown, N. R., Frantz, C. W., Lumadue, M. R., and Cannon, F.:

637 Effects of pyrolysis temperature on the chemical composition of refined

638 softwood and hardwood lignins, Carbon, 60, 531-537,

639 https://doi.org/10.1016/j.carbon.2013.04.087, 2013.

640 Frisch, M. J., Trucks, G. W., Schlegel, H. B., Scuseria, G. E., Robb, M. A.,

641 Cheeseman, J. R., Scalmani, G., Barone, V., Petersson, G. A., Nakatsuji,

642 H., Li, X., Caricato, M., Marenich, A. V., Bloino, J., Janesko, B. G.,

643 Gomperts, R., Mennucci, B., Hratchian, H. P., Ortiz, J. V., Izmaylov, A.

644 F., Sonnenberg, J. L., Williams, Ding, F., Lipparini, F., Egidi, F., Goings,

645 J., Peng, B., Petrone, A., Henderson, T., Ranasinghe, D., Zakrzewski, V.

646 G., Gao, J., Rega, N., Zheng, G., Liang, W., Hada, M., Ehara, M., Toyota,

647 K., Fukuda, R., Hasegawa, J., Ishida, M., Nakajima, T., Honda, Y., Kitao,

648 O., Nakai, H., Vreven, T., Throssell, K., Montgomery Jr., J. A., Peralta,

649 J. E., Ogliaro, F., Bearpark, M. J., Heyd, J. J., Brothers, E. N., Kudin, K.

650 N., Staroverov, V. N., Keith, T. A., Kobayashi, R., Normand, J.,

651 Raghavachari, K., Rendell, A. P., Burant, J. C., Iyengar, S. S., Tomasi,

652 J., Cossi, M., Millam, J. M., Klene, M., Adamo, C., Cammi, R.,

653 Ochterski, J. W., Martin, R. L., Morokuma, K., Farkas, O., Foresman, J.

654 B., and Fox, D. J.: Gaussian 16 Rev. C.01 [code], 2016.

655 Gao, Y., Li, G., Qin, Y., Ji, Y., Mai, B., and An, T.: New theoretical insight

656 into indirect photochemical transformation of fragrance nitro-musks:

657 Mechanisms, eco-toxicity and health effects, Environ Int, 129, 68-75,

658 https://doi.org/10.1016/j.envint.2019.05.020, 2019.

659 Grassian, V. H.: New Directions: Nanodust – A source of metals in the

660   atmospheric environment?, Atmos Environ, 43, 4666-4667,

661   https://doi.org/10.1016/j.atmosenv.2009.06.032, 2009.

662 Hawthorne, S. B., Krieger, M. S., Miller, D. J., and Mathiason, M. B.:

663   Collection and quantitation of methoxylated phenol tracers for

664   atmospheric pollution from residential wood stoves, Environ. Sci.

665   Technol., 23, 470-475, https://doi.org/10.1021/es00181a013, 1989.

666 Henry, F., Coeur-Tourneur, C., Ledoux, F., Tomas, A., and Menu, D.:

667   Secondary organic aerosol formation from the gas phase reaction of

668   hydroxyl radicals with m-, o- and p-cresol, Atmos Environ, 42, 3035-

669   3045, https://doi.org/10.1016/j.atmosenv.2007.12.043, 2008.

670 Hub, J. S., de Groot, B. L., and van der Spoel, D.: g_wham—A Free

671   Weighted Histogram Analysis Implementation Including Robust Error

672   and Autocorrelation Estimates, J. Chem. Theory Comput., 6, 3713-3720,

673   10.1021/ct100494z, 2010.

674 Humphrey, W., Dalke, A., and Schulten, K.: VMD: Visual molecular

675   dynamics, J Mol Graph Model, 14, 33-38, https://doi.org/10.1016/0263-

676   7855(96)00018-5, 1996.

677 Ito, A. and Penner, J. E.: Historical emissions of carbonaceous aerosols from

678   biomass and fossil fuel burning for the period 1870–2000, Global

679   Biogeochem Cy, 19, https://doi.org/10.1029/2004GB002374, 2005.

680 Jämbeck, J. P. and Lyubartsev, A. P.: Update to the general amber force field

681   for small solutes with an emphasis on free energies of hydration, J Phys

682   Chem B, 118, 3793-3804, https://doi.org/10.1021/jp4111234, 2014.

683   Jiang, W., Niedek, C., Anastasio, C., and Zhang, Q.: Photoaging of phenolic

684   secondary organic aerosol in the aqueous phase: evolution of chemical

685   and optical properties and effects of oxidants, Atmos. Chem. Phys., 23,

686   7103-7120, https://doi.org/10.5194/acp-23-7103-2023, 2023.

687   Kroflič, A., Huš, M., Grilc, M., and Grgić, I.: Underappreciated and

688   Complex Role of Nitrous Acid in Aromatic Nitration under Mild

689   Environmental Conditions: The Case of Activated Methoxyphenols,

690   Environ. Sci. Technol., 52, 13756-13765,

691   https://doi.org/10.1021/acs.est.8b01903, 2018.

692   Kumar, S., Rosenberg, J. M., Bouzida, D., Swendsen, R. H., and Kollman,

693   P. A.: THE weighted histogram analysis method for free-energy

694   calculations on biomolecules. I. The method, J Comput Chem, 13, 1011-

695   1021, https://doi.org/10.1002/jcc.540130812, 1992.

696   Kusaka, R., Nihonyanagi, S., and Tahara, T.: The photochemical reaction of

697   phenol becomes ultrafast at the air–water interface, Nat Chem, 13, 306-

698   311, https://doi.org/10.1038/s41557-020-00619-5, 2021.

699   Lee, J. K., Banerjee, S., Nam, H. G., and Zare, R. N.: Acceleration of

700   reaction in charged microdroplets, Q. Rev. Biophys., 48, 437-444,

701   https://doi.org/10.1017/S0033583515000086, 2015a.

702   Lee, J. K., Kim, S., Nam, H. G., and Zare, R. N.: Microdroplet fusion mass

703   spectrometry for fast reaction kinetics, PANS, 112, 3898-3903,

704   https://doi.org/10.1073/pnas.1503689112, 2015b.

705 Liao, Y., Koelewijn, S.-F., Van den Bossche, G., Van Aelst, J., Van den Bosch,

706   S., Renders, T., Navare, K., Nicolaï, T., Van Aelst, K., Maesen, M.,

707   Matsushima, H., Thevelein, J. M., Van Acker, K., Lagrain, B.,

708   Verboekend, D., and Sels, B. F.: A Sustainable Wood Biorefinery for

709   Low-Carbon Footprint Chemicals Production, Science, 367, 1385-1390,

710   https://doi.org/10.1126/science.aau1567, 2020.

711 Liu, C., Chen, D., and Chen, X. e.: Atmospheric Reactivity of

712   Methoxyphenols: A Review, Environ. Sci. Technol., 56, 2897-2916,

713   https://doi.org/10.1021/acs.est.1c06535, 2022.

714 Liu, C., Liu, J., Liu, Y., Chen, T., and He, H. J. A. e.: Secondary organic

715   aerosol formation from the OH-initiated oxidation of guaiacol under

716   different experimental conditions, Atmos Environ, 207, 30-37,

717   https://doi.org/10.1016/j.atmosenv.2019.03.021, 2019.

718 Lou, R., Wu, S.-b., and Lv, G.-j.: Effect of conditions on fast pyrolysis of

719   bamboo   lignin,   J   Anal   Appl   Pyrol,   89,   191-196,

720   https://doi.org/10.1016/j.jaap.2010.08.007, 2010.

721 Lu, T. and Chen, F.: Multiwfn: A multifunctional wavefunction analyzer, J

722   Comput Chem, 33, 580-592, https://doi.org/10.1002/jcc.22885, 2012.

723 Lu, T. and Chen, Q.: Interaction Region Indicator: A Simple Real Space

724   Function   Clearly   Revealing   Both   Chemical   Bonds   and   Weak

725 Interactions**, Chemistry–Methods, 1, 231-239,

726 https://doi.org/10.1002/cmtd.202100007, 2021.

727 Nollet, H., Roels, M., Lutgen, P., Van der Meeren, P., and Verstraete, W.:

728 Removal of PCBs from wastewater using fly ash, Chemosphere, 53,

729 655-665, https://doi.org/10.1016/S0045-6535(03)00517-4, 2003.

730 Platt, U. F., Winer, A. M., Biermann, H. W., Atkinson, R., and Pitts, J. N.:

731 Measurement of nitrate radical concentrations in continental air, Environ.

732 Sci. Technol., 18, 365-369, https://doi.org/10.1021/es00123a015, 1984.

733 Prinn, R., Weiss, R., Miller, B., Huang, J., Alyea, F., Cunnold, D., Fraser, P.,

734 Hartley, D., and Simmonds, P.: Atmospheric Trends and Lifetime of

735 CH_3CCl_3 and Global OH Concentrations, Science,

736 https://doi.org/10.1126/science.269.5221.187, 1995a.

737 Prinn, R. G., Weiss, R. F., Miller, B. R., Huang, J., Alyea, F. N., Cunnold, D.

738 M., Fraser, P. J., Hartley, D. E., and Simmonds, P. G.: Atmospheric

739 Trends and Lifetime of CH_3CCl_3 and Global OH Concentrations,

740 Science, 269, 187-192, https://doi.org/10.1126/science.269.5221.187,

741 1995b.

742 Qu, Z.-w. and Kroes, G.-J.: Theoretical Study of the Electronic Structure

743 and Stability of Titanium Dioxide Clusters $(TiO_2)_n$ with n = 1−9, J Phys

744 Chem B, 110, 8998-9007, https://doi.org/10.1021/jp056607p, 2006.

745 Rana, M. S. and Guzman, M. I.: Oxidation of Phenolic Aldehydes by Ozone

746 and Hydroxyl Radicals at the Air–Water Interface, J Phys Chem A, 124,

747   8822-8833, https://doi.org/10.1021/acs.jpca.0c05944, 2020.

748 Reid, J. S., Eck, T. F., Christopher, S. A., Koppman, R., Dubovik, O.,

749   Eleuterio, D. P., Holben, B. N., Reid, E. A., and Zhang, J.: A review of

750   biomass burning emissions part III: Intensive optical properties of

751   biomass burning particles, Atmos. Chem. Phys., 5, 827-849,

752   https://doi.org/10.5194/acp-5-827-2005, 2005.

753 Roeselová, M., Vieceli, J., Dang, L. X., Garrett, B. C., and Tobias, D. J.:

754   Hydroxyl Radical at the Air−Water Interface, J. Am. Chem. Soc., 126,

755   16308-16309, https://doi.org/10.1021/ja045552m, 2004.

756 Rogge, W. F., Hildemann, L. M., Mazurek, M. A., and Cass, G. R.: Sources

757   of Fine Organic Aerosol. 9. Pine, Oak, and Synthetic Log Combustion

758   in Residential Fireplaces, Environ. Sci. Technol., 32, 13-22,

759   https://doi.org/10.1021/es960930b, 1998.

760 Rubasinghege, G., Elzey, S., Baltrusaitis, J., Jayaweera, P. M., and Grassian,

761   V. H.: Reactions on Atmospheric Dust Particles: Surface Photochemistry

762   and Size-Dependent Nanoscale Redox Chemistry, J. Phys. Chem. Lett.,

763   1, 1729-1737, https://doi.org/10.1021/jz100371d, 2010.

764 Sakata, K., Takahashi, Y., Takano, S., Matsuki, A., Sakaguchi, A., and

765   Tanimoto, H.: First X-ray Spectroscopic Observations of Atmospheric

766   Titanium Species: Size Dependence and the Emission Source, Environ.

767   Sci. Technol., 55, 10975-10986, https://doi.org/10.1021/acs.est.1c02000,

768   2021.

769 Shang, H., Wang, X., Li, H., Li, M., Mao, C., Xing, P., Zhao, S., Chen, Z.,

770   Sun, J., Ai, Z., and Zhang, L.: Oxygen vacancies promote sulfur species

771   accumulation on TiO$_2$ mineral particles, Appl. Catal. B Environ., 290,

772   120024, https://doi.org/10.1016/j.apcatb.2021.120024, 2021.

773 Shi, Q., Zhang, W., Ji, Y., Wang, J., Qin, D., Chen, J., Gao, Y., Li, G., and

774   An, T.: Enhanced uptake of glyoxal at the acidic nanoparticle interface:

775   implications for secondary organic aerosol formation, Environ Sci-Nano,

776   7, 1126-1135, https://doi.org/10.1039/D0EN00016G, 2020.

777 Simoneit, B. R. T.: Biomass burning — a review of organic tracers for

778   smoke from incomplete combustion, Appl Geochem, 17, 129-162,

779   https://doi.org/10.1016/S0883-2927(01)00061-0, 2002.

780 Smith, J. D., Kinney, H., and Anastasio, C.: Phenolic carbonyls undergo

781   rapid aqueous photodegradation to form low-volatility, light-absorbing

782   products, Atmos Environ, 126, 36-44,

783   https://doi.org/10.1016/j.atmosenv.2015.11.035, 2016.

784 Soongprasit, K., Sricharoenchaikul, V., and Atong, D.: Phenol-derived

785   products from fast pyrolysis of organosolv lignin, Energy Rep, 6, 151-

786   167, https://doi.org/10.1016/j.egyr.2020.08.040, 2020.

787 Sun, J., Han, D., Shallcross, D. E., Cao, H., Wei, B., Mei, Q., Xie, J., Zhan,

788   J., and He, M.: Theoretical studies on the heterogeneous ozonolysis of

789   syringol on graphene: Mechanism, kinetics and ecotoxicity assessment,

790   Chem. Eng.J., 404, 126484, https://doi.org/10.1016/j.cej.2020.126484,

791   2021a.

792   Sun, N., Rodríguez, H., Rahman, M., and Rogers, R. D.: Where are ionic

793   liquid strategies most suited in the pursuit of chemicals and energy from

794   lignocellulosic   biomass?,   Chem.   Commun.,   47,   1405-1421,

795   https://doi.org/10.1039/C0CC03990J, 2011.

796   Sun, Y., Chen, X., Liu, L., Xu, F., and Zhang, X.: Mechanisms and kinetics

797   studies of the atmospheric oxidation of eugenol by hydroxyl radicals and

798   ozone   molecules,   Sci   Total   Environ,   770,   145203,

799   https://doi.org/10.1016/j.scitotenv.2021.145203, 2021b.

800   Syzgantseva, O. A., Gonzalez-Navarrete, P., Calatayud, M., Bromley, S.,

801   and Minot, C.: Theoretical Investigation of the Hydrogenation of $(TiO_2)_n$

802   Clusters (N = 1–10), J Phys Chem C, 115, 15890-15899,

803   https://doi.org/10.1021/jp2050349, 2011.

804   Wang, R., Li, K., Li, J., Tsona, N. T., Wang, W., and Du, L.: Interaction of

805   Acrylic Acid and SO2 on the Surface of Mineral Dust Aerosol, Acs Earth

806   Space   Chem,   7,   548-558,

807   https://doi.org/10.1021/acsearthspacechem.2c00323, 2023.

808   Yan, X., Bain, R. M., and Cooks, R. G.: Organic Reactions in Microdroplets:

809   Reaction Acceleration Revealed by Mass Spectrometry, Angew. Chem.

810   Int. Ed., 55, 12960-12972, https://doi.org/10.1002/anie.201602270,

811   2016.

812   Yao, L., Yang, L., Chen, J., Wang, X., Xue, L., Li, W., Sui, X., Wen, L., Chi,

813   J., Zhu, Y., Zhang, J., Xu, C., Zhu, T., and Wang, W.: Characteristics of

814   carbonaceous aerosols: Impact of biomass burning and secondary

815   formation in summertime in a rural area of the North China Plain, Sci

816   Total   Environ,   557-558,   520-530,

817   https://doi.org/10.1016/j.scitotenv.2016.03.111, 2016.

818   Yee, L. D., Kautzman, K. E., Loza, C. L., Schilling, K. A., Coggon, M. M.,

819   Chhabra, P. S., Chan, M. N., Chan, A. W. H., Hersey, S. P., Crounse, J.

820   D., Wennberg, P. O., Flagan, R. C., and Seinfeld, J. H.: Secondary

821   organic aerosol formation from biomass burning intermediates: Phenol

822   and   methoxyphenols,   Atmos.   Chem.   Phys.,   13,   8019-8043,

823   https://doi.org/10.5194/acp-13-8019-2013, 2013.

824   Zein, A. E., Coeur, C., Obeid, E., Lauraguais, A., and Fagniez, T.: Reaction

825   Kinetics of Catechol (1,2-Benzenediol) and Guaiacol (2-Methoxyphenol)

826   with   Ozone,   J   Phys   Chem   A,   119,   6759-6765,

827   https://doi.org/10.1021/acs.jpca.5b00174, 2015.

828   Zhai, H.-J. and Wang, L.-S.: Probing the Electronic Structure and Band Gap

829   Evolution of Titanium Oxide Clusters $(TiO2)n-$ $(n = 1-10)$ Using

830   Photoelectron Spectroscopy, J. Am. Chem. Soc., 129, 3022-3026,

831   https://doi.org/10.1021/ja068601z, 2007.

832   Zhang, W., Ji, Y., Li, G., Shi, Q., and An, T.: The heterogeneous reaction of

833   dimethylamine/ammonia with sulfuric acid to promote the growth of

834   atmospheric   nanoparticles,   Environ   Sci-Nano,   6,   2767-2776,

835   https://doi.org/10.1039/C9EN00619B, 2019.

836   Zhang, W., Tong, S., Jia, C., Wang, L., Liu, B., Tang, G., Ji, D., Hu, B., Liu,

837   Z., Li, W., Wang, Z., Liu, Y., Wang, Y., and Ge, M.: Different HONO

838   Sources for Three Layers at the Urban Area of Beijing, Environ. Sci.

839   Technol., 54, 12870-12880, https://doi.org/10.1021/acs.est.0c02146,

840   2020.

841   Zhong, J., Kumar, M., Anglada, J. M., Martins-Costa, M. T. C., Ruiz-Lopez,

842   M. F., Zeng, X. C., and Francisco, J. S.: Atmospheric Spectroscopy and

843   Photochemistry at Environmental Water Interfaces, Annu Rev Phys

844   Chem, 70, 45-69, https://doi.org/10.1146/annurev-physchem-042018-

845   052311, 2019.

846

847
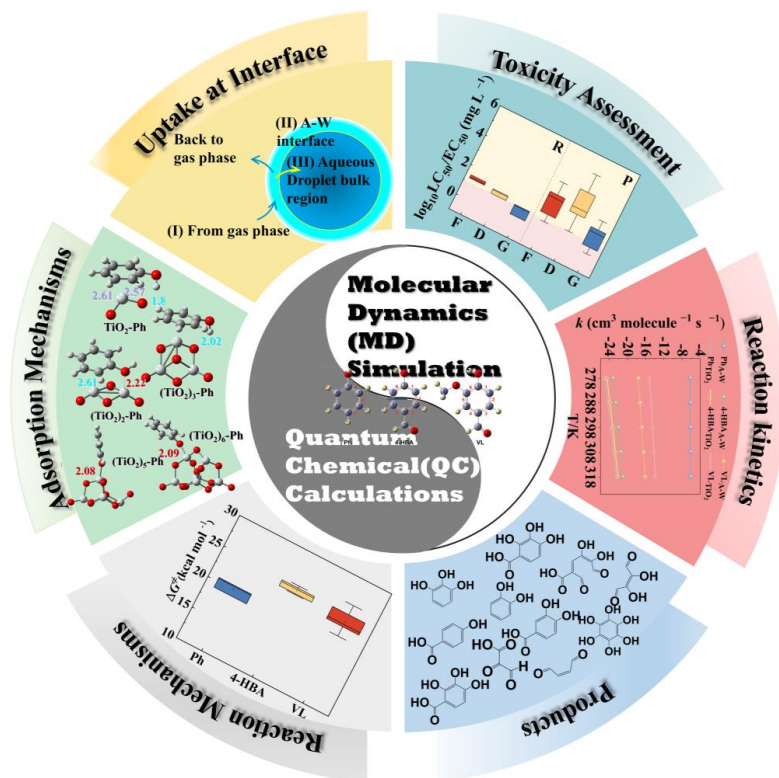
848 *Graphical Abstract*

849

850

851

852

853

854

855

856

857
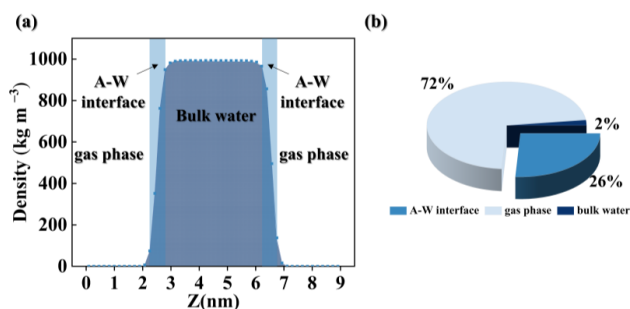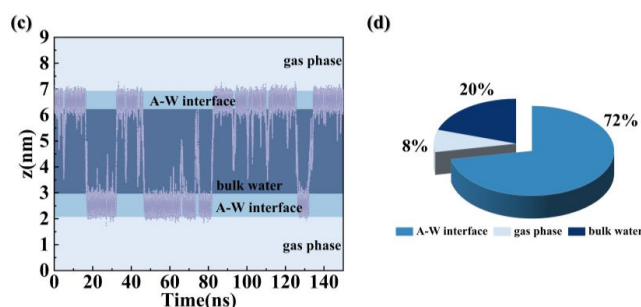
Fig.1 (a) Relative concentration distributions in the A-W system along the z-axis; **(b)** probability of

O_3 at the A-W interface, in gas phase, and in bulk water; **(c)** MD trajectories of Ph diffusion through

the water slab over a 150 ns period; **(d)** probability of Ph at the A-W interface, in gas phase, and in
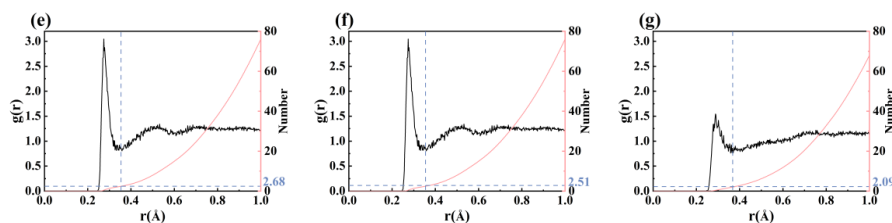
bulk water.
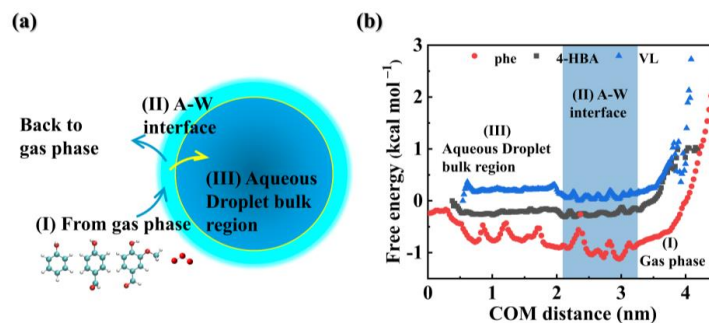
Fig.2 (a) Three key processes for the reaction of gaseous PhCs (Ph, 4-HBA, or VL) with the

nanoparticles; **(b)** free energy profile of gaseous PhCs (Ph, 4-HBA, or VL) approaching the bulk

water.
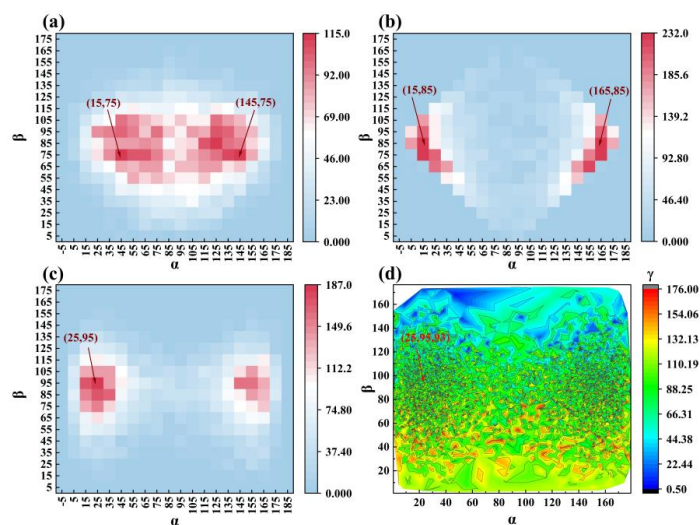
868

869

870 **Fig. 3** Angle (α, β, γ) distribution probability of **(a)** Ph, **(b)** 4-HBA, or **(c)** VL with respect to A-W

871 interface; radial distribution function (RDF) and the coordination number N of **(e)** H_{Ph-OH}-O_{H_2O}, **(f)**

872 $H_{4-HBA-OH}$-O_{H_2O}, and **(g)** H_{VL-OH}-O_{H_2O} at the A-W interface.
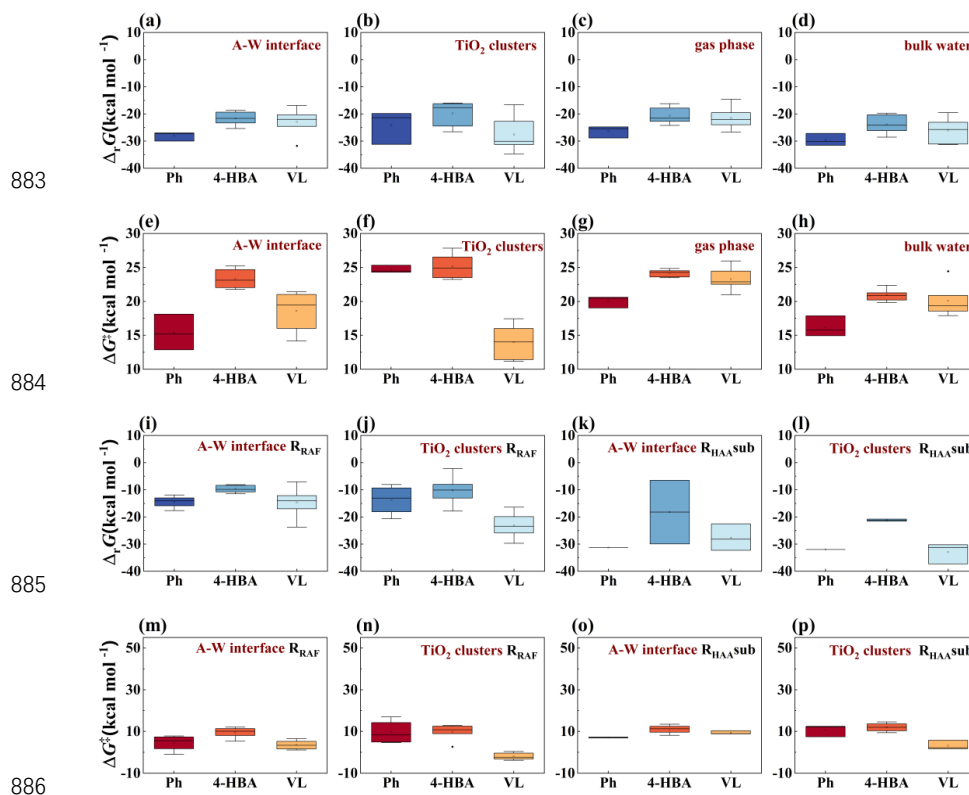
873

874

875

876
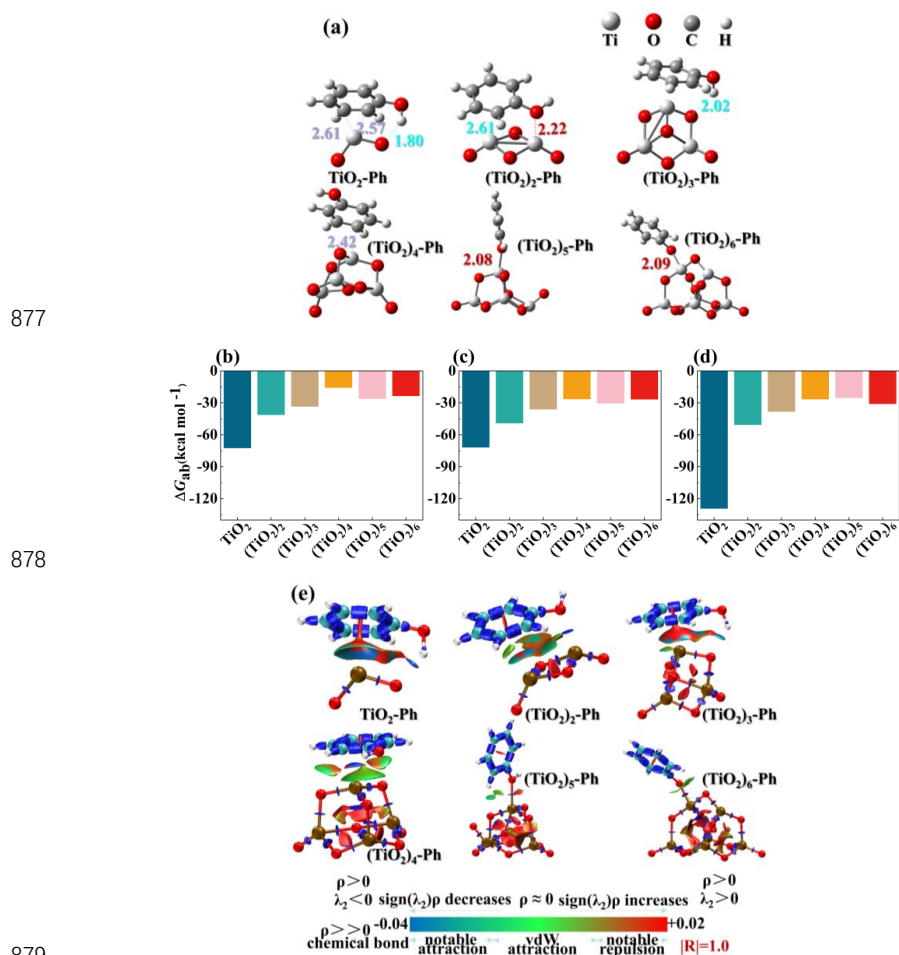
Fig. 4 Adsorption details of PhCs on $(TiO_2)_n$ (n = 1−6) clusters; **(a)** structure of Ph adsorption on $(TiO_2)_n$ (n = 1−6) surface; adsorption energy of **(b)** Ph, **(c)** 4-HBA, and **(d)** VL on $(TiO_2)_n$ (n = 1−6, unit: kcal mol^{-1}); **(e)** Interaction region indicator (IRI) analyses of Ph on $(TiO_2)_n$ (n = 1−6) surface.
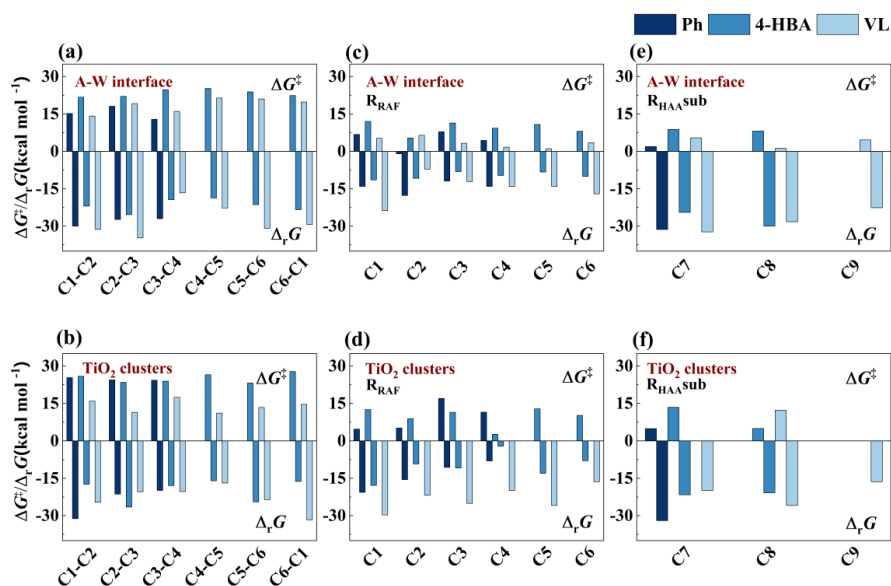
Fig. 5 Statistical charts of calculated **(a)**–**(d)** $\Delta_r G$ and **(e)**–**(h)** $\Delta G^{\ddagger}$ values for O_3-initiated reactions;

(i)–**(l)** $\Delta_r G$ and **(m)**–**(p)** $\Delta G^{\ddagger}$ values for $HO^{\bullet}$-initiated reactions.

Fig.6 $\Delta_r G$ and $\Delta G^\ddagger$ values of **(a)–(b)** O_3-initiated reactions and **(c)–(f)** $HO^\bullet$-initiated reactions at

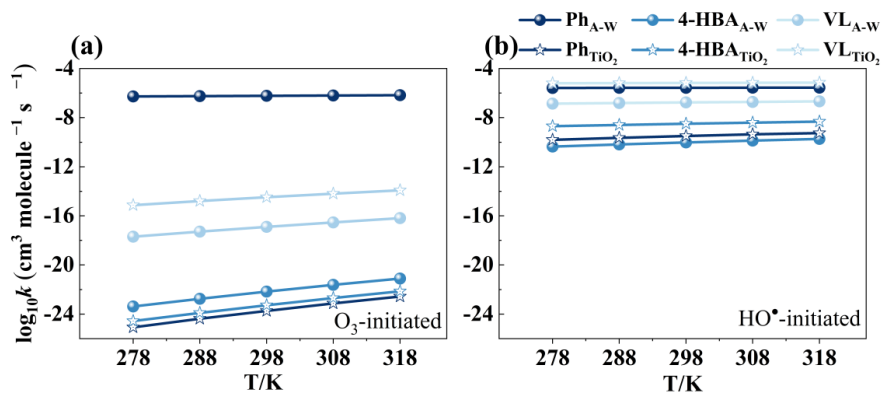different reaction positions.

46

(a)

892

(b)

893
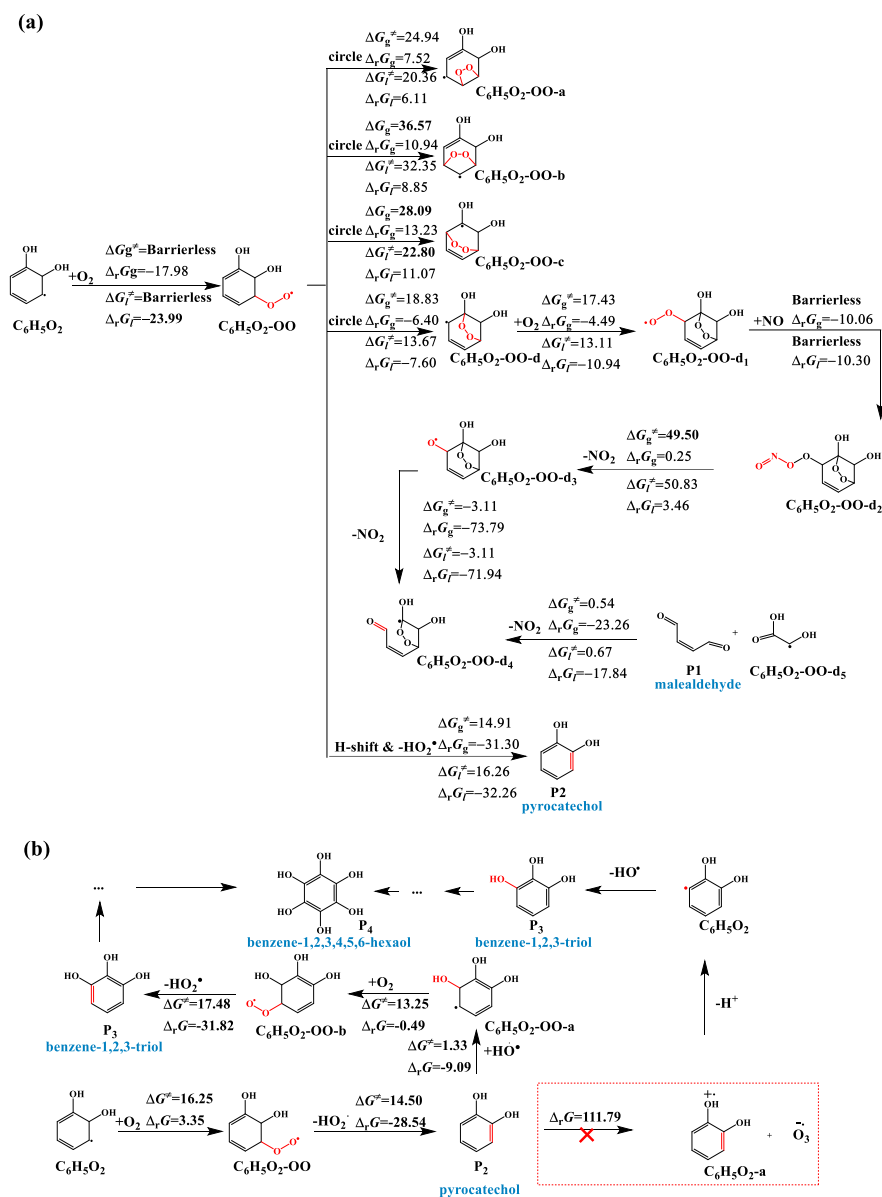
Fig.7 Subsequent reaction mechanisms of important intermediates (IMs) (unit: kcal mol^{-1}) in **(a)**

gas phase / bulk water and at **(b)** A-W interface.

896

897

Fig.8 Calculated rate constants for the initial reactions of Ph, 4-HBA, and VL with O_3 and $HO^{\bullet}$ at different temperatures (278–318 K) and 1 atm.

915 **Table 1** The available experimental and calculated reaction rate constants (k) values of O_3-

916 initiated and $HO^\bullet$-initiated reactions at 298 K. Unit: cm^3 molecule $^{-1}$ s $^{-1}$.

Compounds	$k_{tot\text{-}A\text{-}W,\text{cal}}$[a]	$k_{tot\text{-}TiO_2,\text{cal}}$[b]	$k_{tot\text{-}gas,\text{cal}}$[c]	$k_{tot\text{-}wat,\text{cal}}$[d]	$k_{,\exp}$	Ref.
Ph	5.98×10^{-7}	1.84×10^{-24}	5.27×10^{-20}	4.02×10^{12}	$(13.5 \pm 1.1) \times 10^{-18,\,e}$	Zein et al. (2015)
	2.69×10^{-6}	3.17×10^{-10}	2.34×10^{-9}	4.46×10^{13}	—	
4-HBA	6.79×10^{-23}	5.32×10^{-24}	4.93×10^{-24}	1.97×10^{12}	—	
	9.49×10^{-11}	3.16×10^{-9}	7.90×10^{-11}	2.52×10^{13}	—	Rana et al. (2020)
VL	1.27×10^{-17}	3.30×10^{-15}	1.35×10^{-22}	2.20×10^{12}	$(0.40 \pm 0.31) \times 10^{-18,\,f}$	Zein et al. (2015)
	1.73×10^{-7}	6.70×10^{-6}	1.14×10^{-10}	3.15×10^{13}	$6.00 \times 10^{-11,\,g}$	Rana et al. (2020)

917 [a]: calculated values of phenolic compounds at A-W interface;

918 [b]: calculated values of phenolic compounds on TiO_2 clusters;

919 [c]: calculated values of phenolic compounds in the gas phase;

920 [d]: calculated values of phenolic compounds in the bulk water.

921 [e]: experimental values of catechol in the gas phase;

922 [f]: experimental values of guaiacol in the gas phase;

923 [g]: experimental average $k_{HO\bullet}$ values of methoxyphenols in the gas phase.